



HAL
open science

High-pressure, halogen-bearing melt preserved in ultrahigh-temperature felsic granulites of the Central Maine Terrane, Connecticut (U.S.A.)

Silvio Ferrero, Jay Ague, Patrick O'brien, Bernd Wunder, Laurent Remusat, Martin A Ziemann, Jennifer Axler, Patrick J O'Brien

► To cite this version:

Silvio Ferrero, Jay Ague, Patrick O'brien, Bernd Wunder, Laurent Remusat, et al.. High-pressure, halogen-bearing melt preserved in ultrahigh-temperature felsic granulites of the Central Maine Terrane, Connecticut (U.S.A.). *The American Mineralogist*, 2021, 106 (8), pp.1225-1236. 10.2138/am-2021-7690 . hal-03402462

HAL Id: hal-03402462

<https://hal.science/hal-03402462>

Submitted on 25 Oct 2021

HAL is a multi-disciplinary open access archive for the deposit and dissemination of scientific research documents, whether they are published or not. The documents may come from teaching and research institutions in France or abroad, or from public or private research centers.

L'archive ouverte pluridisciplinaire **HAL**, est destinée au dépôt et à la diffusion de documents scientifiques de niveau recherche, publiés ou non, émanant des établissements d'enseignement et de recherche français ou étrangers, des laboratoires publics ou privés.

1 **High pressure, halogen-bearing melt preserved in ultra-high temperature felsic granulites**
2 **of the Central Maine Terrane, Connecticut (US)**

3 Silvio Ferrero^{1,2}, Jay Ague³, Patrick J. O'Brien¹, Bernd Wunder⁴, Laurent Remusat⁵, Martin A.
4 Ziemann¹, Jennifer Axler⁶

5
6 ¹ *Universität Potsdam, 14476 Potsdam, Germany*

7 ² *Museum für Naturkunde (MfN), Leibniz-Institut für Evolutions-und Biodiversitätsforschung,*
8 *10115 Berlin, Germany*

9 ³ *Yale University, New Haven, CT, 06520-8109, US*

10 ⁴ *Helmholtz-Zentrum Potsdam, GFZ, D-14473 Potsdam, Germany*

11 ⁵ *Museum National d'Histoire Naturelle, Paris*

12 ⁶ *Wellesley College, 106 Central Street – Wellesley, MA 02481*

13
14 **Abstract**

15 Inclusions of high pressure melts provide crucial information on the fate of crustal rocks in the
16 deep roots of collisional orogens during collision and crustal thickening, often at rather extreme
17 conditions, e.g. temperatures in excess of 1000°C. However, findings of this type are still a
18 relative rarity among case studies of MI in metamorphic rocks. Here we present the results of the
19 experimental and microchemical investigation of nanogranitoids in garnets from the felsic
20 granulites of the Central Maine Terrane (Connecticut, US). Their successful experimental re-
21 homogenization at almost 2 GPa confirms that they originally were trapped portions of deep
22 melts and makes them the first direct evidence of high pressure during peak metamorphism and
23 melting for these felsic granulites. The trapped melt has a hydrous, granitic and peraluminous

24 character typical of crustal melts from metapelites. This melt is higher in mafic components (FeO
25 and MgO) than most of the nanogranitoids investigated so far, likely the result of the extreme
26 melting temperatures – well above 1000°C. This is the first natural evidence of the positive
27 correlation between temperature and mafic character of the melt, a trend previously supported
28 only by experimental evidence. Moreover it poses a severe *caveat* against the common
29 assumption that partial melts from metasediments at depths are always leucogranitic in
30 composition.

31 NanoSIMS measurement on re-homogenized inclusions show significant amounts of CO₂, Cl and
32 F. Halogens abundance in the melt is considered a proxy for the presence of brines, strongly
33 saline fluids, at depth. Brines are known to shift the melting temperatures of the system toward
34 higher values, and may have been responsible for delaying melt production via biotite
35 dehydration melting until these rocks reached extreme temperatures of more than 1000°C, rather
36 than 800-850°C as commonly observed for these reactions.

37 **Keywords**

38 High pressure granulites, anatexis, nanogranitoids, carbon, halogens, piston cylinder

39

INTRODUCTION

40
41 The investigation of melt inclusions in felsic (Ferrero et al., 2015; Cesare et al., 2015) and
42 mafic (Ferrero et al., 2018a) granulites is the most straightforward approach to the investigation
43 of melting processes in the lower continental crust, directly in their source region. These droplets
44 of anatectic melt are generally partially to totally crystallized, i.e. as nanogranitoids due to the
45 slow cooling of the host rock (Ferrero et al., 2012; Cesare et al., 2015). They contain a
46 cryptocrystalline aggregate of phases consistent with the crystallization of a silicate rich melt
47 (Ferrero et al., 2018b). The expected phases include, but they are not limited to, OH-bearing
48 phases, quartz and feldspar(s) or their metastable polymorphs (Ferrero et al., 2016). Just like fluid
49 and mineral inclusions, melt inclusions in metamorphic rocks are tools for natural scientists to
50 peer into the history of the host rocks, obtain geochemical information on deep processes, and to
51 better constrain P-T-t-X history of the rock (Ferrero and Angel, 2018).

52 Multiphase inclusions with features consistent with nanogranitoids were reported by Ague and
53 Axler (2015) in garnets from layers of sillimanite-rich rocks hosted in gneisses of the Central
54 Maine Terrane (CMT - Acadian orogeny, NE Connecticut, US). Phase assemblages in the
55 inclusions and microstructures classify them as former droplets of melt trapped during garnet
56 formation at the metamorphic peak, $\sim 1050^{\circ}\text{C}$ and ≥ 1 GPa (Axler and Ague, 2015). The host rock
57 has attracted considerable interest in recent years because of its very high T of re-equilibration at
58 relatively low P (including cordierite-spinel assemblages), allowing Ague et al. (2013) to
59 interpret them as the first example of ultrahigh temperature (*UHT*) metamorphic rocks in North
60 America. By definition, *UHT* metamorphism involves T in excess of 900°C achieved along
61 apparent geothermal gradient $\geq 20^{\circ}\text{C}/\text{Km}$ (Brown, 2006), i.e. mostly in the stability field of
62 sillimanite. *UHT* metamorphism has been to date identified in dozens of localities worldwide,

63 mostly in Precambrian rocks (Kelsey, 2008), although much younger *UHT* rocks, i.e. Miocene in
64 age, have been also recently reported (Pownall et al., 2018). More recent studies of other rocks in
65 the CMT document high-pressure granulite facies metamorphism (~1050 °C, ~1.8 GPa) of silica-
66 undersaturated garnet-spinel-corundum gneisses (Keller and Ague, 2018), as well as UHP
67 metamorphism (Keller and Ague, 2020).

68 Piston cylinder re-homogenization followed by in situ characterization is a common and well-
69 established approach for nanogranitoids studies to follow in order to (1) prove that they originally
70 were indeed droplets of melt, and (2) characterize geochemistry and fluid content and speciation
71 content of anatectic melt (e.g. Acosta-Vigil et al., 2016; Bartoli et al., 2016; Carvalho et al., 2018;
72 Bartoli et al., 2019). Our detailed experimental and microchemical work confirmed that the CMT
73 multiphase inclusions were originally a hydrous and halogen-rich granitic melt formed at T in
74 excess of 1000°C, the hottest preserved melt so far found in natural metasedimentary protolith.
75 Our approach leads to surprising outcomes with broad significance in terms of melt composition
76 and melting processes in the deepest parts of orogenic root zones, as well as of regional
77 geodynamic evolution.

78 **METHODS**

79 Our study involved the use of a piston cylinder press, back-scattered-electron (BSE) imaging,
80 electron probe analyses (EPMA), energy-dispersive-spectrometry (EDS) elemental mapping and
81 micro-Raman spectroscopy. Several garnet chips with unexposed nanogranitoids of both equant
82 and tubular shape were manually separated from doubly-polished thick sections and used as
83 starting material in re-homogenization experiments. The chips were loaded in a platinum capsule
84 then filled with silica powder, without adding water. The capsules were kept at in a Johannes-
85 type piston-cylinder apparatus at GFZ-Potsdam at variable T and P conditions for up to 24 hours.

86 The temperature in the capsule was controlled using a Type S thermocouple (Pt-PtRh10) with a
87 ± 10 °C uncertainty, while the accuracy of the pressure (P) measurement is estimated to be ± 0.05
88 GPa. Quenching of the experimental charge took place at high P , and the machine was unloaded
89 only after reaching ambient temperature. In-situ analyses were then performed on capsules
90 mounted in epoxy and polished to expose re-homogenized inclusions (for further details see
91 Bartoli et al. 2013b; Ferrero et al. 2015).

92 The Field Emission Gun electron microprobe (FEG-EMP) JEOL Hyperprobe JXA-8500F
93 available at the Natural History Museum of Berlin was used to acquire high-resolution BSE
94 images and EDS elemental maps on nanogranitoids and re-homogenized inclusions. The glass
95 resulting from re-homogenization was analyzed using a JEOL JXA-8200 EMP at Potsdam
96 University. Analytical conditions were similar to previous studies of nanogranitoids (Ferrero et
97 al. 2012; 2015) at 15 kV, 3.5 nA and beam diameter of 1 μm to avoid contamination from the
98 surrounding host. Alkali loss correction factors were estimated using haplogranitic standards
99 (Morgan and London, 2005) and are in the range 17-23% relative for Na_2O and 10-13 % relative
100 for K_2O depending on the analytical session.

101 Fluorine, CO_2 , and H_2O analyses were performed via Nano Secondary Ion Mass Spectrometry
102 (NanoSIMS) using the Cameca NanoSIMS 50 operated at the Muséum National d'Histoire
103 Naturelle of Paris following the procedure described in Bartoli et al. (2014) and Créon et al.
104 (2018). Polished capsules with re-homogenized inclusions on the garnet surface were mounted in
105 Indium along with standard glasses, and the inclusions identified through images of $^{28}\text{Si}^-$ and
106 $^{56}\text{Fe}^{16}\text{O}^-$ secondary ions. Pre-sputtering on a $5 \times 5 \mu\text{m}^2$ surface area for 2 min preceded each
107 analysis in order to remove gold coating, surface contamination and achieve a steady-state
108 sputtering regime. A 20 pA Cs^+ primary beam was used for data acquisition via rastering of a 3×3

109 μm^2 surface area. Ions were exclusively collected from the inner $1 \times 1 \mu\text{m}^2$ (using the beam
110 blanking mode) to minimize surface contamination. Each analysis comprised 200 cycles with a
111 duration of 1.024 s. Secondary ions of $^{12}\text{C}^-$, $^{16}\text{OH}^-$ (proxy for H_2O), $^{19}\text{F}^-$, $^{28}\text{Si}^-$ and $^{56}\text{Fe}^{16}\text{O}^-$ were
112 recorded simultaneously in multicollection mode, using electron multipliers with a dead time of
113 44 ns. Mass resolution was set to 5500 to resolve any mass interference on the selected ions. Only
114 analyses with a stable $^{16}\text{OH}^-/^{28}\text{Si}^-$ ratio were considered in this study. Three glasses of
115 leucogranitic composition and known concentrations of H_2O , varying between ~ 0.3 and 4.86
116 wt% were used for calibration (see Supplementary material). For F concentration, we used NIST
117 610 and 612 standards to determine $[\text{F}]/[\text{SiO}_2]$ ratios from $^{19}\text{F}^-/^{28}\text{Si}^-$. Four trachyandesitic
118 standards (STR 9, 10, 11 and 13) were used to correct for carbon measurements (Créon et al.,
119 2018): these are glass fragments of shoshonite lava from the Stromboli volcano that were
120 experimentally doped in carbon and water by Bureau et al. (2003). Analytical uncertainty on each
121 NanoSIMS measurement (based on the Poisson error due to counting statistics) was combined
122 with the uncertainty on the calibration (corresponding to 66% interval of confidence) by
123 quadratic sum to obtain the 66% uncertainty on values reported in Table 3.

124 Micro-Raman spectroscopy was performed using a HORIBA Jobin Yvon LabRAM HR 800
125 located at the Institute of Geoscience, University of Potsdam. An air-cooled Nd:YAG laser was
126 used for excitation ($\lambda = 532 \text{ nm}$, laser power on the sample of 2–3 mW) with a grating of 300
127 lines/mm, slit width and confocal hole set to 100 μm and 200 μm , respectively. The Raman
128 spectra of re-homogenized glass inclusions as well as crystal phases were acquired with a 100 \times
129 objective in the wavenumber range 100–4000 cm^{-1} , integrating 3 repetitions of 60 s with spectral
130 resolution of 10 cm^{-1} . Raman maps were obtained integrating 2 repetitions of 30 s in 4 spectral

131 windows on each point of the mapped area. Different phases were visualized in the map by color
132 coding of the indexed Raman bands of the phases (cf. O'Brien & Ziemann, 2008).

133

134 **PETROGRAPHIC FEATURES OF THE STARTING MATERIAL**

135 The host rocks are rusty schists characterized by the assemblage garnet+sillimanite+K-
136 feldspar+plagioclase+quartz+cordierite+biotite (Fig.1a). The sillimanite is commonly found as
137 pseudomorphs after kyanite. Detailed information on sample location and petrographic features
138 are in Axler and Ague (2015). The inclusions occur in the inner part of garnet porphyroblasts
139 with a random distribution indicative of a primary nature, i.e. they formed during growth of the
140 host garnet (Fig. 1b; see also Ferrero et al., 2012). They vary in shape from isometric with
141 diameter $\leq 10 \mu\text{m}$ (Fig. 1c) to needles with length $\leq 100 \mu\text{m}$ and few μm across (Fig. 1d). The
142 latter type is by far the most common in each cluster, a shape never before observed in such
143 abundance in case studies of nanogranitoid, more commonly isometric (Ferrero et al., 2018b;
144 Cesare et al., 2015). The most elongated inclusions show often cracks of limited extension at the
145 corners, evidence of decrepitation. The detailed microchemical and microstructural investigation
146 of the inclusions performed by Axler and Ague (2015) showed that, before the experimental runs,
147 they contain a rather constant assemblage consisting of quartz, phlogopite, white mica and, very
148 often, a compositionally variable phase (CV phase in Axler and Ague 2015) interpreted as
149 residual glass.

150 Raman investigation (Fig. 2a) and mapping of isometric inclusions shows that cristobalite is
151 present instead of quartz in some inclusions (Fig. 2b) and coexists with two micas and accessory
152 phases such as apatite and ilmenite (Fig. 2c, d, e), whereas no inclusion show the presence of
153 residual glass. However, the Raman map shows a crystalline phase with main peaks at 292, 430

154 and 479 cm^{-1} , assigned to a still unidentified and possibly new phase (hence “phase 430”) already
155 found and analyzed in nanogranitoids from HP/UHP rocks of the Bohemian Massif, and having
156 composition similar to a granitic glass. Graphite occurs as mineral inclusions in garnet and
157 occasionally as a trapped phase in the inclusions. A prominent feature of the host garnet is the
158 presence of abundant rutile and ilmenite needles dominantly oriented parallel to $\langle 111 \rangle$ of garnet.
159 Interestingly, needle-shaped nanogranitoids are oriented in the same directions, and typically
160 contain rutile and /or ilmenite as trapped phases.

161 RESULTS

162 Multiple re-homogenization experiments were performed at $T=1050^\circ\text{C}$ and variable confining
163 P, in the range 1.0 – 2.0 GPa (details on experimental runs and products are in Table 1; P-T
164 conditions of each experiment are summarized in Fig. 3). The experimental conditions were
165 chosen to be as close as possible to the conditions of formation, estimated to be $\approx 1040^\circ\text{C}$ based
166 on Zr-in-Rt thermometry on the rutile needles present along with nanogranitoids in the garnet
167 core (Axler and Ague, 2015). The T estimates were calculated assuming 1 GPa as formation P of
168 the host garnet and melt entrapment, thus representing a minimum value (Ague et al., 2013).

169 Each experiment shows complete re-melting of the inclusions, i.e. no leftovers of the original
170 phases in the nanogranitoids are visible after the heating run, with the exception of clearly
171 trapped accessories such as rutile and ilmenite. The absence of embayments and regular linear
172 walls in the inclusions rules out that garnet dissolved into the melt (Ferrero et al., 2012; Bartoli et
173 al., 2013), as expected in case of significant overheating during the experiments, i.e. the chosen
174 temperature is likely very close to the liquidus of the trapped melt. However, the experiments
175 performed at $P < 1.7\text{ GPa}$ (numbers 1, 2 in fig. 3) constantly show formation of new garnet,
176 higher in Mg than the original host phase (Figs. 4a,b,c,d) and occasionally small orthopyroxene

177 crystals identified via Raman spectroscopy at $P \leq 1.2$ GPa. Moreover, at 1 GPa most inclusions
178 show extensive evidence of decrepitation (Fig. 4a). The two experiments performed at 1.7 and
179 2.0 GPa (numbers 3 and 4 respectively, Fig. 3) do show fully re-homogenized glassy inclusions
180 without evidence of decrepitation and/or formation of new phases (Figs. 4e,f,g,h,i).

181

182 **Melt composition**

183 The glass measured in the inclusions after successful experimental re-homogenization is
184 hydrous, granitic (Fig. 5a,b) and very K-rich (av. $K_2O/Na_2O = 3.89$, Table 2), with a clear
185 peraluminous ($ASI = 1.22$, Fig. 6c) and alkalic to alkali-calcic character (Fig. 5d). Importantly,
186 such melts are not leucogranitic, as commonly expected for anatectic melts from melting of
187 metasediments: they have indeed a rather high FeO+MgO content (4.05 wt%; 4.27 wt% when
188 recalculated on an anhydrous basis; Table 2). The presence of H_2O in the glass is visible in
189 Raman spectra acquired on re-homogenized nanogranitoids, which show the broad band of water
190 in the region $3200-3800\text{ cm}^{-1}$ (Fig. 6).

191 The H_2O content of the melt, along with CO_2 and F, was measured in garnets from experiment
192 #3 and #4 using NanoSIMS. One single inclusion shows very low values of all three volatile
193 species, suggesting that it may have lost most of its volatiles possibly as result of decrepitation
194 during quenching (measurement Exp3_MI_1 in Table 3) and thus it is not further considered in
195 the average values calculated below. The volatiles were quantified as 4.40 wt% H_2O , 3072 ppm
196 CO_2 and 3161 ppm F on average (Fig.7a). With the exclusion of the single analysis discussed
197 above, H_2O content in the rest of the dataset is rather consistent (Fig. 7a), whereas the CO_2 and F
198 contents of the melt vary by an order of magnitude (Figure 7a; Table 3) depending on the
199 inclusion (Fig. 7b, c). Interestingly, EMPA measurements on the re-homogenized inclusions

200 show that Cl is also present in remarkable amounts, reaching almost 1 wt%, with average 0.32
201 wt%, making this melt more enriched in halogens (Cl, F) than any previous anatectic melt so far
202 investigated in nanogranitoids.

203

204

DISCUSSION

205 The present study targets polycrystalline inclusions in garnet from felsic granulites of the
206 Central Maine Terrane. Our results confirm that they are volumes of crystallized melt trapped
207 during garnet growth at the metamorphic peak, as already proposed based on mineralogical and
208 microstructural investigation by Axler and Ague (2015). Raman investigation shows the presence
209 of metastable cristobalite, i.e. formed outside its stability field (see e.g. Hwang et al., 2004). The
210 occurrence of metastable polymorphs in nanogranitoids has been interpreted as direct evidence
211 that the inclusions preserve their original composition, as these phases recrystallize to their most
212 common counterparts (i.e. quartz) when the inclusions decrepitate, i.e. becomes an open system,
213 able to exchange components with the rock matrix via cracks in the host garnet (Ferrero et al.,
214 2016). Such inclusions therefore offer access to unaltered deep melts still preserved in the natural
215 rock which underwent melting at depth (Ferrero and Angel, 2018).

216 The investigation of CMT nanogranitoids thus provides a detailed portrait of formation
217 conditions, geochemistry, and volatile content of melt from metasediments at crustal depth. The
218 extremely high T at which the melt was produced is rather close to the Bt-out curve according to
219 the melting experiments on metasediments of Auzeanneau et al. (2006). Indeed the peraluminous
220 and granitic nature of the re-homogenized melt, its relatively low amount of H₂O and its
221 occurrence in (peritectic) garnet are all features consistent with melt generated by biotite
222 dehydration melting (LeBreton and Thompson, 1988), with residual biotite still locally visible as

223 mineral inclusions (Fig. 1a). Furthermore, the enrichment in chlorine and fluorine of the trapped
224 melt is likely to influence the stability of the biotite (see discussion in the paragraph “volatiles in
225 high pressure melt”).

226 The composition measured in the re-homogenized inclusions, especially its granitic character
227 and the high K/Na ratio ($\approx 4:1$) is consistent with the phase assemblage, which always includes
228 quartz/cristobalite plus two K-bearing phases (muscovite and phlogopite). The phase 430
229 identified via Raman investigation is likely to be the “phase CV”, reported in these inclusions by
230 Axler and Ague (2015) and interpreted as residual glass because of their granitic-like
231 composition: the narrow peaks visible in its Raman spectrum however clearly belongs to a
232 crystalline rather than a glass phase. Moreover, very similar compositions to the one reported by
233 Ague and Axler (2015) were measured in phase 430 from garnet pyroxenites from the
234 Granulitgebirge (Bohemian Massif; unpublished EMP data; Ferrero et al., in preparation), thus
235 making this phase the main Na repository in the targeted nanogranitoids.

236 A peculiarity of this case study is represented by the shape of the inclusions. Most case studies
237 of nanogranitoids show inclusions with a more or less developed negative crystal shape, the
238 response of host garnet to the need of lowering the surface free energy of the melt-garnet
239 interface and move toward textural equilibration (Ferrero et al., 2012). Instead tubular/acicular
240 shapes in nanogranitoids are not unheard of (Ferrero et al, 2012; Cesare et al., 2015) but they are
241 overall a rarity. CMT nanogranitoids are a rather unique case as the acicular shape, i.e. defined by
242 an extreme elongation/width ratio, characterizes the majority of the inclusions (Fig. 1b,c). So far
243 only the polycrystalline inclusions in the garnet megacrysts of Gore Mountain in the Adirondacks
244 (Darling et al., 1997) show similar features, although in the latter case only ~50% of the
245 inclusions have such shape (Ferrero and Angel, 2018). Further investigations are needed to

246 understand the reasons underlying the dichotomy negative-crystal versus acicular shape in
247 inclusions from different localities.

248 The original rationale at the base of our work was two-folds: verifying the former melt nature
249 of the inclusions and obtaining the bulk composition of the original melt. The study however
250 generated three most unexpected results: (a) re-homogenization experiments show that this melt
251 formed under high pressure (*HP*) conditions, in contrast with previous studies of these felsic
252 granulites; (b) whereas the melt itself is peraluminous and granitic in composition, rather
253 common features in melts from metasediments, it shows an unexpected high mafic (FeO+MgO)
254 component; (c) in terms of volatiles, the melt contains significant amounts of halogens (Cl, F)
255 besides typical species observed in silicate melts, e.g. H₂O and CO₂.

256

257 **First evidence of *HP* in the felsic granulites of the Central Maine Terrane**

258 Possibly the most consequential result of our study is that the inclusions re-homogenize
259 completely in equilibrium with the host garnet only at $P \geq 1.7$ GPa, considerably in excess of the
260 minimum of 1.0 GPa as originally expected based on the estimates of Ague et al. (2013) and
261 Axler and Ague (2015). Garnet growth conditions and thus MI entrapment coincide with those of
262 partial melting, as both garnet and melt are products of the same melting reaction (Cesare et al.,
263 2015 and references therein), and are under chemical equilibrium during their formation. Thus,
264 successful re-homogenization experiments on nanogranitoids are a completely independent tool
265 to constrain the PT conditions of garnet formation in presence of melt (Ferrero et al., 2018b).
266 Both P and T still need to be calculated beforehand using independent methods, e.g.
267 thermodynamic modeling and classic geothermobarometry on the metamorphic assemblage to
268 which the inclusion-bearing garnet belongs, in order to proceed with the experiments. If the

269 calculated formation conditions are correct, (most of) the nanogranitoids should re-melt
270 completely without reacting with the host during the experimental run (see Bartoli et al. 2013a,b;
271 Acosta-Vigil et al., 2016; Ferrero et al., 2015; 2016; 2018b; Borghini et al. 2018). Conversely,
272 textural evidence of melt-garnet disequilibrium as well as decrepitation evidence would indicate
273 the experimental parameters were not representative of the formation conditions. As an example,
274 the critical evaluation of the nanogranitoid microstructures after heating experiments at different
275 P allowed Ferrero et al. (2018b) to bracket the P conditions of melting of the felsic granulites of
276 Orlica–Śnieżnik Dome (OSD; Bohemian Massif) to 2.7 ± 0.1 GPa, starting from an initial range
277 of calculated P spanning from 1.8 to 3.0 GPa based on previous geothermobarometric and
278 modelling studies.

279 Our detailed experimental work on the CMT nanogranitoids shows that the nanogranitoids re-
280 melt at $T=1050^\circ\text{C}$. At 1.0 GPa the abundance of decrepitation cracks in the re-melted inclusions
281 is a clear evidence of insufficient confining P , which leads to failure of the container (the garnet)
282 due to inclusion overpressurization during the heating run. Moreover, all the experiments at P
283 <1.7 GPa show evidence of chemical disequilibrium between the newly produced glass and the
284 surrounding garnet. This causes melt-garnet interaction, with formation of new phases not present
285 in the inclusions before experimental runs, e.g. orthopyroxene and/or change in composition
286 (Mg-increase) of the garnet around the inclusion. Newly formed, Mg-richer garnet was also
287 reported in nanogranitoids from the OSD felsic granulites after experiments at P lower than those
288 of melt formation (Ferrero et al., 2018). Hence the microstructural appearance of the CMT
289 nanogranitoids after reheating show an evolution similar to that reported in Ferrero et al. (2018b),
290 with the Mg-rich garnet disappearing once the confining P reaches 1.7 GPa, thus suggesting that
291 both garnet and melt formed at $P \geq 1.7$ GPa.

292

293 **High mafic content in pristine anatectic melt from metasediments**

294 Granitic melts with geochemistry similar to the CMT nanogranitoids, i.e., high ASI index,
295 rather high normative orthoclase and high FeO+MgO, are reported from experiments on natural
296 metapelitic rocks at 1 GPa and 1025-1075 °C (Patiño-Douce and Johnston, 1991) and in
297 nanogranitoid from metapelitic migmatites which experienced UHT conditions, 950°C and 0.5
298 GPa, in the Kerala Khondalite Belt, Southern India (Cesare et al., 2009; Ferrero et al., 2012; see
299 table 2 and fig. 8a,b for the whole nanogranitoid and experimental dataset). It may be argued that
300 such a mafic-rich character is the result of contamination between glass and host, as the
301 inclusions are hosted in Fe- and Mg-rich garnet (Axler and Ague, 2015). However, contamination
302 via (even limited) dissolution of garnet during re-heating experiments can be excluded based on
303 microstructural basis, i.e. the inclusions show regular shapes and lack embayments indicative of
304 melt-garnet interaction. Contamination during EMPA analysis can be also ruled out for the
305 inclusions selected for EMPA investigation and reported in Table 2. The size of the re-
306 homogenized inclusions was sufficiently large (>5 µm in diameter) to avoid the excitation
307 volume created by the electron beam (diameter 1 µm) to come in contact with the host. In the few
308 cases where the inclusions were ≤5 µm, garnet contamination was clearly visible as the measured
309 SiO₂ showed a sharp decrease, coupled with FeO increase (Fig. 8a). As microstructural evidence
310 of garnet dissolution was completely absent from these small inclusions, we ascribed this
311 phenomenon to the fact that the excitation volume created by the beam also included a portion of
312 the host. Analyses from inclusions below 4-5 µm were then removed from the dataset
313 (contaminated analyses are given in the supplementary material). Based on such considerations,

314 the high mafic component of the melt preserved in these felsic granulites should be considered a
315 primary feature.

316 CMT nanogranitoids have a very high average FeO+MgO content when compared with
317 experimental melts from metasedimentary protoliths, i.e. 4.27 wt% in the CMT nanogranitoids
318 versus 0.9-3.9 wt% of the experimental dataset when taken on anhydrous basis, as compiled by
319 Stevens et al. (2007). The database of nanogranitoids and melt inclusions (Bartoli et al., 2016)
320 shows that most of the melt inclusions (for a total of ~600 analyses in 2016) show a
321 FeO+MgO+TiO₂ content in the range 0.25-2.50 wt%, with only ~10% of the whole database
322 having contents 4 - 5 wt%. As CMT nanogranitoids show an average FeO+MgO+TiO₂ =4.63
323 wt% (Table 2), their mafic component is higher than almost 90% of the anatectic melt inclusions
324 measured so far.

325 Experimental work on Fe and Mg contents in haplogranitic melts (Johannes and Holtz, 1996)
326 and melting experiments on metasediments (Patiño-Douce and Johnston, 1991; Montel and
327 Vielzeuf, 1997; Droop et al., 2003) show that a granitic melt produced during melting of
328 metasediments can accommodate a progressively higher amount of Fe and Mg as the formation T
329 of the melt increases. Such observations, so far rooted exclusively in experimental findings, are
330 now supported by our natural data. This is clearly visible when they are plotted against data
331 available in literature on granitic inclusions from metasediments melted at different T (Fig. 7; see
332 also Table 2). Different case studies of nanogranitoids show a positive correlation between
333 melting T (corresponding in turn to melt entrapment in the growing host) and FeO+MgO content.
334 Indeed, the melt in the CMT nanogranitoids, which shows the highest FeO+MgO content among
335 all the granitic inclusions, formed at $T \geq 1000^\circ\text{C}$, the highest formation T identified so far in

336 nanogranitoids from metasediments. Conversely, the melt produced at lower T , 700-710°C,
337 shows the lowest FeO+MgO content, in the range 1.34-1.83 wt%.

338 A variable degree of FeO+MgO enrichment is commonly observed in S-type (anatexis-related)
339 granites (e.g. Stevens et al., 2007; Villaros et al., 2009) and in leucosomes and small granite
340 sheets associated with migmatite bodies with sedimentary protoliths, coupled to increases in
341 A/CNK and decreases in silica content (Taylor and Stevens, 2012). This has been proposed to be
342 the result of selective entrainment in the magma of peritectic garnet, possibly the most common
343 repository of Fe, Mg and Al in metamorphosed crustal rocks, as the melt progressively coalesces
344 at depth and migrates upwards (Stevens et al., 2007). This hypothesis assumes that most pristine
345 anatectic melts from metasediments are leucogranitic and very low in mafic components, a
346 concept so far supported by both experiments (Stevens et al., 2007) and melt inclusions (Bartoli
347 et al., 2016). However, our study proves that anatectic melts can instead show a rather high
348 content of Fe and Mg when produced at $T > 1000^\circ\text{C}$ and, thus, they should be considered to have a
349 pristine, “starting” composition (Ferrero et al., 2012; Bartoli et al., 2016). This observation does
350 not affect the validity of the peritectic phase entrainment hypothesis, which remains a sound
351 explanation for FeO+MgO enrichment in S-type granites. It does however pose a significant
352 caveat for researchers who want to correctly estimate the magnitude of peritectic phase
353 entrainment experienced by the granitic body/leucosome under investigation, warning in
354 particular against overestimating the magnitude of entrainment by assuming a too small
355 FeO+MgO content in the original anatectic melt when the latter is produced at T in excess of
356 950-1000 °C.

357

358 **Volatiles in high pressure melt**

359 H₂O is necessary to stabilize any silicate melt under crustal conditions, and the quantification of
360 H₂O, as well as of other species such as CO₂ and halogens, partitioned into deep partial melts is
361 of utmost importance for quantifying volatile cycles at depth and how they affect deep melting
362 processes (Bartoli et al., 2014). NanoSIMS analyses on re-homogenized nanogranitoids is a
363 routine approach in nanogranitoid studies (e.g. Acosta-Vigil et al. 2016), and it has shown that
364 nanogranitoids generally preserve their original composition in terms of H₂O (Bartoli et al., 2014)
365 and CO₂ contents (Carvalho et al., 2019). In particular, the loss of H₂O (even as OH) from the
366 inclusion to the matrix surrounding the garnet would shift the liquidus of the trapped melt toward
367 higher T (Johannes and Holtz, 1996). Thus the nanogranitoids would re-homogenize only at *T*
368 significantly higher than those obtained via independent geothermobarometry on the host rocks,
369 which is not the case here: the inclusions re-homogenize indeed at ~1050°C, consistently with the
370 *T* range of Zr-in-Rt thermometers on the rutile needles present in the nanogranitoid-bearing
371 garnets (Axler and Ague, 2015). In this work, the average H₂O value (4.40 wt%) is rather close to
372 that obtained via difference from 100 of the EMP totals after alkali loss correction (4.63 wt%).
373 Both values are consistent with experimental estimates of H₂O content in haplogranitic melts at
374 the PT conditions of interest, as the experimental parameters of the two successful experiments
375 (point 3 and 4 in Fig. 2) are close to the 4 wt% H₂O liquidus curve extrapolated at P >1.0 GPa
376 (Johannes and Holtz, 1996).

377 The melt also contains significant amounts of CO₂, on average ~ 3000 ppm (0.3 wt%). This
378 CO₂ may be internally produced as result of the devolatilization of hydrous silicates in the
379 presence of graphite (Connolly and Cesare, 1993; Cesare et al., 2005) visible in the CMT felsic
380 granulites as trapped minerals in inclusions and/or as mineral inclusions in garnet and the rock
381 matrix (Axler and Ague 2015). The CO₂ content of the CMT nanogranitoids is higher, on

382 average, than in the nanogranitoids measured in the graphite-bearing metasediments of the Ivrea-
383 Verbano Zone (IVZ; Carvalho et al., 2019), the only other case study so far where CO₂ was
384 measured in situ in re-homogenized nanogranitoids. It is likely that the different depth at which
385 melting occurred played a major role in shaping the CO₂ content of the melt. Experimental
386 studies have shown that CO₂ solubility in melt increases dramatically with increasing P (~500
387 ppm each 0.1 GPa in experimental studies; Ni and Keppler, 2013), and in fact our results show
388 that CMT nanogranitoids likely formed at significantly greater depth than IVZ nanogranitoids,
389 1.7-2.0 GPa (this study) vs. 0.8 GPa (Carvalho et al., 2019).

390 Probably the most striking feature of the CMT melt is the presence of a significant amount of
391 halogens. Chlorine (0.32 wt% average) and F (3161 ppm, or ~0.32 wt%) account together for
392 0.64 wt% on average of the total melt composition. This is also consistent with the fact that
393 phlogopite crystallized inside the CMT nanogranitoids has been found, in one case, to contain an
394 unusually high amount of F (>1 wt%; Axler and Ague, 2015). Halogens are characteristic of
395 brines, i.e. saline and Cl-rich fluid with low H₂O activity, proposed by some authors to play an
396 important role in the melting processes occurring in a thickened crust at either lower crustal or
397 upper mantle conditions (Aranovich et al., 2014). The Cl content of partial melts can be used as
398 proxy for the presence of brines during melt production at depth (Acosta-Vigil et al., 2016). CMT
399 nanogranitoids contain 0.10-0.98 wt% of Cl, an amount comparable to those reported in
400 experimental melts coexisting with brines, i.e., ranging between ~0.2 and 1.6 wt% (Webster and
401 Mandeville, 2007; Aranovich et al., 2013; Safonov et al., 2014). Experiments show furthermore
402 that brines in a haplogranitic system may cause a significant shift of the minimum melting *T*
403 toward higher values due to the lowering of the H₂O activity (Aranovich et al., 2013), thus
404 helping to create the conditions for melting to occur at extreme temperatures (>1000°C) as

405 proposed for the CMT felsic granulites, a notion independently supported by both previous PT
406 estimates (Ague et al., 2013; Axler and Ague, 2015) as well as by the complete re-
407 homogenization of the nanogranitoids at 1050°C. Another possibility is that the enrichment in
408 halogens predated the metamorphic peak, i.e. the brines were not present during melting but had
409 infiltrated the felsic granulites during their prograde metamorphic evolution. In this scenario, Cl
410 and F are incorporated in the biotite, and this process extends biotite stability field toward UHT
411 conditions (Martin and Hand, 2015), thus allowing biotite to destabilize at significantly higher T
412 than commonly expected.

413 **IMPLICATIONS and CONCLUSIONS**

414 The deep nature of granulite metamorphism and the high thermal flux required to achieve
415 melting favor post-melting re-equilibration and re-crystallization of granulites/migmatites, often
416 obliterating the most direct evidence of the presence of melt, such as leucosomes and melt
417 pseudomorphs (White et al., 2011). For this reason the preserved melt inclusions sheltered in
418 peak peritectic garnet of the CMT felsic granulites are a crucial finding. They indeed provide new
419 data necessary to a more comprehensive portrait of the multiple aspects of melting, melt
420 preservation, and crustal evolution during metamorphism in the deep roots of orogens. In
421 particular:

422 • HP melts from metasediments are still underrepresented in the nanogranitoid database, as
423 the bulk of the reported case studies of nanogranitoids are from rocks melted at $P < 1.5$ GPa (see
424 lists in Cesare et al., 2015; Bartoli et al., 2016; Acosta-Vigil et al., 2016; Ferrero et al. 2018b).
425 The only two case studies of melts produced at $P > 1.5$ GPa are from significantly greater depths
426 of 2.7 GPa (Ferrero et al. 2015) and > 4.5 GPa (Stepanov et al 2016). Along with the recent work
427 on the metasomatic nanogranitoids hosted in the Granulitgebirge pyroxenites (Borghini et al.,

428 2018; 2020), our data are a step toward filling the gap in knowledge on natural partial melts
429 forming at intermediate P (~2.0 GPa). A further important feature of CMT nanogranitoids is the
430 fact that they are richer in mafic components (FeO and MgO) than the majority of nanogranitoid
431 case studies. Their pristine nature thus provides a direct confirmation that the granitic melt from
432 anatexis can accommodate an increasing amount of Fe and Mg with increasing T, an observation
433 rooted until now exclusively in experimental studies. This finding is thus a caveat against
434 assuming that natural pristine anatectic melts are always leucogranitic.

435 • Our independent experimental results provide the first evidence of HP conditions during
436 the metamorphic peak / melting of the felsic granulites in the Central Maine Terrane, pointing
437 toward melting conditions of ~1050°C and 1.7-2.0 GP. HP metamorphism, rather than purely
438 UHT (Ague et al., 2013), is also supported by the widespread presence of pseudomorphs of
439 sillimanite after kyanite in the matrix (Axler and Ague, 2015). Our findings warrants a
440 reappraisal of the metamorphic peak conditions in the area and finds direct support in other recent
441 studies in nearby localities: HP conditions (1.8 GPa) reported in silica-undersaturated gneisses
442 (Keller and Ague, 2018), whereas other metapelites contain evidence of UHP metamorphism (>5
443 GPa; Keller and Ague, 2020);

444 • H₂O, CO₂, Cl and F were measured directly in situ in the HP crustal melt still preserved in
445 its original source rock. H₂O was so far measured in nanogranitoids from rocks equilibrated
446 between ~0.4 GPa and 1.4 GPa (Bartoli et al., 2014; 2016; Acosta-Vigil et al., 2016; Carvalho et
447 al., 2019), whereas CO₂ in situ measurements are only available from the IVZ, equilibrated at 0.8
448 GPa (Carvalho et al. 2019). Our new measurements extend the existent dataset toward
449 significantly greater depth and provide the foundation of further studies to further clarify how the
450 interplay of protolith, fluid speciation, and PT conditions influence H₂O and carbon budgets

451 during crustal subduction and thickening. Moreover, to our knowledge our study presents the first
452 data on F measured in situ in anatectic melt inclusions. Previous experimental studies suggest that
453 the presence of a significant amount of Cl such as the one measured in the CMT inclusions may
454 be indicative of the presence of saline fluids, e.g. brine, during melting. This is the first direct
455 natural evidence that brines infiltrating the lower crust as a metasomatic fluid may be an
456 influential factor for the establishment of conditions necessary to produce melt at such extreme
457 temperatures (>1000°C), commonly inferred to be characterized by fluid-absent melting
458 conditions.

459

460 Acknowledgements

461 The present research was funded by the German Federal Ministry for Education and Research
462 and the Deutsche Forschungsgemeinschaft (Project FE 1527/2-1 and FE 1527/2-2) to SF. JJA
463 gratefully acknowledges support from the National Science Foundation (EAR-1250269 and
464 EAR-1753553) and Yale University. The NanoSIMS facility at the Muséum National d'Histoire
465 Naturelle in Paris was established by funds from the CNRS, Région Ile de France, Ministère
466 délégué à l'Enseignement supérieur et à la Recherche, and the Muséum National d'Histoire
467 Naturelle. Our deepest thanks go to C. Günter, F. Kaufmann and L. Hecht for help during
468 analyses, and to C. Fischer for sample preparation.

469

470 *References*

471 Acosta-Vigil, A., Barich, A., Bartoli, O., Garrido, C.J., Cesare, B., Remusat, L., Poli, S.,
472 and Raepsaet, C. (2016). The composition of nanogranitoids in migmatites overlying the Ronda
473 peridotites (Betic Cordillera, S Spain): the anatectic history of a polymetamorphic basement.
474 *Contributions to Mineralogy and Petrology*, 171, 24.

475 Acosta-Vigil, A., Cesare, B., London, D., Morgan, G. B., VI (2007). Microstructures and
476 composition of melt inclusions in a crustal anatexis environment, represented by metapelitic
477 enclaves within El Hoyazo dacites, SE Spain. *Chemical Geology* 235, 450-465.

478 Aranovich, L.Y., Makhlof, A.R., Manning, C.E., and Newton, R.C. (2014) Dehydration melting
479 and the relationship between granites and granulites. *Precambrian Research*, 253, 26–37.

480 Aranovich, L.Y., Newton, R.C., and Manning, C.E. (2013) Brine-assisted anatexis:
481 experimental melting in the system haplogranite–H₂O–NaCl–KCl at deep-crustal conditions.
482 *Earth and Planetary Science Letters* 374, 111-120.

483 Auzanneau, E., Vielzeuf, D., and Schmidt, M.W. (2006) Experimental evidence of
484 decompression melting during exhumation of subducted continental crust. *Contributions to
485 Mineralogy and Petrology*, 152, 125–148.

486 Axler, J.A., and Ague, J.J. (2015) Oriented multiphase needles in garnet from ultrahigh-
487 temperature granulites. *American Mineralogist*, 100, 2254–2271.

488 Bartoli, O., Acosta-Vigil, A., Ferrero, S., and Cesare, B. (2016) Granitoid magmas preserved as
489 melt inclusions in high-grade metamorphic rocks. *American Mineralogist*, 101, 1543–1559.

490 Bartoli, O., Cesare, B., Poli, S., Acosta-Vigil, A., Esposito, R., Turina, A., Bodnar, R.J., Angel,
491 R.J., and Hunter, J. (2013a) Nanogranite inclusions in migmatitic garnet: Behavior during piston
492 cylinder re-melting experiments. *Geofluids*, 13, 405–420.

493 Bartoli, O., Cesare, B., Poli, S., Bodnar, R.J., Acosta-Vigil, A., Frezzotti, M.L., and Meli, S.
494 (2013b) Recovering the composition of melt and the fluid regime at the onset of crustal anatexis
495 and S-type granite formation. *Geology*, 41, 115–118.

496 Bartoli, O., Cesare, B., Remusat, L., Acosta-Vigil, A. and Poli, S. (2014) The H₂O content of
497 granite embryos. *Earth and Planetary Science Letters* 395, 281-290.

498 Bodnar RJ (2003) Reequilibration of fluid inclusions. In I. Samson, A. Anderson, & D.
499 Marshall, eds. *Fluid Inclusions: Analysis and Interpretation*. Mineral. Assoc. Canada, Short
500 Course 32, 213-230.

501 Borghini, A., Ferrero, S., Wunder, B., Laurent, O., O'Brien, P. J., and Ziemann, M. A. (2018)
502 Granitoid melt inclusions in orogenic peridotite and the origin of garnet clinopyroxenite.
503 *Geology*, 46(11), 1007–1010.

504 Borghini, A., Ferrero, S., O'Brien, P. J., Laurent, O., Günter, C., and Ziemann, M. A. (2020)
505 Cryptic metasomatic agent measured in situ in Variscan mantle rocks: Melt inclusions in garnet
506 of eclogite, Granulitgebirge, Germany. *Journal of Metamorphic Geology*, 38, 207–234.

507 Brown, M., 2006. Duality of thermal regimes is the distinctive characteristic of plate
508 tectonics since the Neoproterozoic. *Geology*, 34, 961e964.

509 Bureau, H., Trocellier, P., Shaw, C., Khodja, H., Bolfan-Casanova, N., Demouchy, S., 2003.
510 Determination of the concentration of water dissolved in glasses and minerals using nuclear
511 microprobe. *Nucl. Instrum. Methods Phys. Res., Sect. B* 210, 449–454.

512 Carvalho, B. B., Bartoli, O., Ferri, F., Cesare, B., Ferrero, S., Remusat, L., Capizzi, L.S., Poli,
513 S. (2019). Anatexis and fluid regime of the deep continental crust: New clues from melt and fluid
514 inclusions in metapelitic migmatites from Ivrea zone (NW Italy). *Journal of Metamorphic
515 Geology*, 37, 951-975. 63

516 Connolly, J. A. D. And Cesare, B. (1993) C-O-H-S fluid composition and oxygen fugacity in
517 graphitic metapelites. *Journal of Metamorphic Geology*, 11, 368-378.

518 Cesare, B., Acosta-Vigil, A., Bartoli, O., and Ferrero, S. (2015) What can we learn from melt
519 inclusions in migmatites and granulites? *Lithos*, 239, 186–216.

520 Cesare, B., Meli, S., Nodari, L., and Russo, U., (2005) Fe³⁺ reduction during biotite melting in
521 graphitic metapelites: another origin of CO₂ in granulites. *Contributions to Mineralogy and*
522 *Petrology*, 149, 129–140.

523 Cesare, B., Ferrero, S., Salvioli-Mariani, E., Pedron, D., and Cavallo, A. (2009a) Nanogranite
524 and glassy inclusions: the anatectic melt in migmatites and granulites. *Geology*, 37, 627–630.

525 Créon, L., Levresse, G., Remusat, L., Bureau, H. and Carrasco-Núñez, G. (2018) New method
526 for initial composition determination of crystallized silicate melt inclusions. *Chemical Geology*
527 483, 162-173.

528 Darling, R. S., Chou, I.-M., and Bodnar, R. J. (1997) An occurrence of metastable cristobalite
529 in high-pressure garnet granulite. *Science*, 276, 91–93.

530 Droop, G.T.R., Clemens, J.D., and Dalrymple, J. (2003) Processes and conditions during
531 contact anatexis, melts escape and restite formation: The Huntly Gabbro complex, NE Scotland.
532 *Journal of Petrology*, 44, 995–1029.

533 Ferrero, S., and Angel, R. J. (2018) Micropetrology: are inclusions in minerals grains of truth?
534 *Journal of Petrology*, 59, 1671–1700.

535 Ferrero, S., Bodnar, R.J., Cesare, B., and Viti, C. (2011) Reequilibration of primary fluid
536 inclusions in peritectic garnet from metapelitic enclaves, El Hoyazo, Spain. *Lithos*, 124, 117–
537 131.

538 Ferrero, S., Bartoli, O., Cesare, B., Salvioli-Mariani, E., Acosta-Vigil, A., Cavallo, A., Groppo,
539 C., and Battiston, S. (2012) Microstructures of melt inclusions in anatectic metasedimentary
540 rocks. *Journal of Metamorphic Geology*, 30, 303–322.

541 Ferrero, S., Wunder, B., Ziemann, Wälle, M., and O’Brien, P.J. (2016a) Carbonatitic and
542 granitic melts produced under conditions of primary immiscibility during anatexis in the lower
543 crust. *Earth Planetary Science Letters*, 454, 121–131.

544 Ferrero, S., Ziemann, M.A., Angel, R.J., O’Brien, P.J. and Wunder, P.J. (2016b) Kumdykolite,
545 kokchetavite, and cristobalite crystallized in nanogranites from felsic granulites, Orlica Snieznik
546 Dome (Bohemian Massif): not evidence for ultrahigh pressure conditions. *Contributions to*
547 *Mineralogy and Petrology*, 171, 3.

548 Ferrero, S., Godard, G., Palmeri, R., Wunder, B., and Cesare B. (2018a) Partial melting of
549 ultramafic granulites from Dronning Maud Land, Antarctica: Constraints from melt inclusions
550 and thermodynamic modelling. *American Mineralogist*, 103, 610-622.

551 Ferrero, S., O’Brien, P. J., Borghini, A., Wunder, B., Wälle, M., Günter, C., and Ziemann, M.
552 A. (2018b) A treasure chest full of nanogranitoids: an archive to investigate crustal melting in the
553 Bohemian Massif, in Ferrero, S., Lanari, P., Goncalves, P., and Grosch, E. G., eds., *Metamorphic*
554 *Geology: Microscale to Mountain Belts: Geological Society, London, Special Publications 478,*
555 13-38.

556 Ferrero S, Wunder B, Walczak K, Ziemann MA, O’Brien PJ (2015). Preserved near ultrahigh-
557 pressure melt from continental crust subducted to mantle depths. *Geology*, 43, 447-450.

558 Hauri, E., Wang, J., Dixon, J.E., King, P.L., Mandeville, C. and Newman, S. (2002) SIMS
559 analysis of volatiles in silicate glasses: 1. Calibration, matrix effects and comparisons with FTIR.
560 *Chemical Geology* 183, 99-114.

561 Hwang, S-L., Shen, P., Chu, H-T., Yui, T-F, Liou, J-G., Sobolev, N.V., Zhang, R.Y., Shatsky,
562 V.S., and Zayachkovsky, A.A. (2004) Kokchetavite: a new polymorph of KAlSi₃O₈ from the
563 Kokchetav UHP terrain. *Contributions to Mineralogy and Petrology*, 148: 380–389.

564 Johannes, W., and Holtz, F. (1996) *Petrogenesis and experimental petrology of granitic rocks,*
565 335 p. Berlin, Springer.

566 Le Breton, N., and Thompson, A.B. (1988) Fluid-absent (dehydration) melting of biotite in
567 metapelites in the early stages of crustal anatexis. *Contributions to Mineralogy and Petrology*, 99,
568 226–237.

569 Morgan G.B.VI, and London, D. (2005a) Effect of current density on the electron microprobe
570 analysis of alkali aluminosilicate glasses. *American Mineralogist*, 90, 1131–1138.

571 Montel, J.-M., and Vielzeuf, D. (1997). Partial melting of metagreywackes, Part II.
572 Compositions of minerals and melts. *Contributions to Mineralogy and Petrology*, 128, 176–196.

573 Ni, H., and Keppler, H. (2013). Carbon in silicate melts. *Reviews in Mineralogy &*
574 *Geochemistry*, 75, 251-287.

575 O'Brien, P.J., and Ziemann, M.A. (2008) Preservation of coesite in exhumed eclogite: insights
576 from Raman mapping. *European Journal of Mineralogy*, 20, 827-834.

577 Patiño Douce, A.E., and Johnston, A.D. (1991) Phase equilibria and melt productivity in the
578 pelitic system: implications for the origin of peraluminous granitoids and aluminous granulites.
579 *Contributions to Mineralogy and Petrology* 107, 202–218.

580 Safonov, O.G., Kosova, S.A., and van Reenen, D.D. (2014) Interaction of biotite-amphibole
581 gneiss with H₂O–CO₂–(K, Na)Cl fluids at 550 MPa and 750 and 800 °C: experimental study and
582 applications to dehydration and partial melting in the middle crust. *Journal of Petrology*, 55,
583 2419–2456.

584 Stepanov, A.S., Hermann, J., Rubatto, D., Korsakov, A.V., Danyushevsky, L.V. (2016) Melting
585 History of an Ultrahigh-pressure Paragneiss Revealed by Multiphase Solid Inclusions in Garnet,
586 Kokchetav Massif, Kazakhstan. *Journal of Petrology*, 57, 1531-1554.

587 Stevens, G., Villaros, A., and Moyen, J.-F. (2007) Selective peritectic garnet entrainment as the
588 origin of geochemical diversity in S-type granites. *Geology* 35, 9–12.

589 Taylor, J., and Stevens, G. (2010). Selective entrainment of peritectic garnet into S-type
590 granitic
591 magmas: evidence from Archaean mid-crustal anatectites. *Lithos*, 120, 277–292.

592 Thomen, A., Robert, F. and Remusat, L. (2014) Determination of the nitrogen abundance in
593 organic materials by NanoSIMS quantitative imaging. *Journal of Analytical Atomic*
594 *Spectrometry* 29, 512-519.

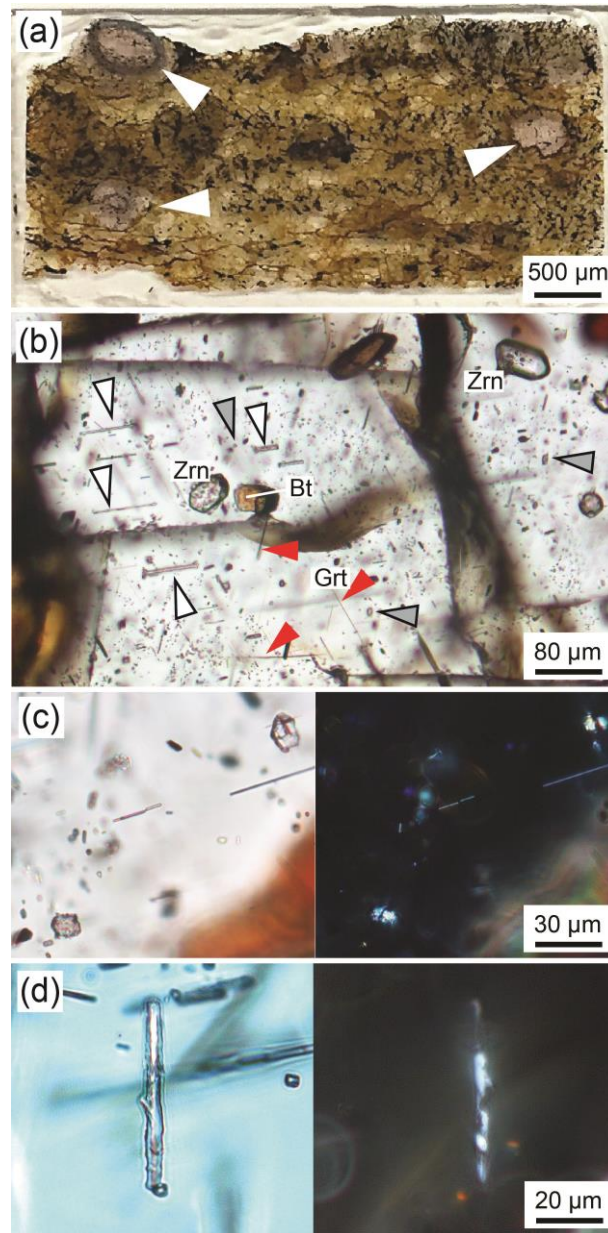
595 Villaros, A., Stevens, G., Moyen, J.F., and Buick, I.S. (2009). The trace element compositions
596 of S-type granites: evidence for disequilibrium melting and accessory phase entrainment in the
597 source. *Contributions to Mineralogy and Petrology*, 158, 543–561.

598 Webster, J.D., and Mandeville, C.W. (2007) Fluid immiscibility in volcanic environments. In:
599 Liebscher A, Heinrich CA (eds) *Fluid-fluid interactions*. *Reviews in Mineralogy and*
600 *Geochemistry*, 65, 313–362.

601 White, R.W., Stevens, G., and Johnson, T.E. (2011) Is the crucible reproducible? Reconciling
602 melting experiments with thermodynamic calculations. *Elements*, 7, 241–246.

603 Whitney, D.L., and Evans, B.W. (2010) Abbreviations for names of rock-forming minerals.
604 *American Mineralogist*, 95, 185–187.

605

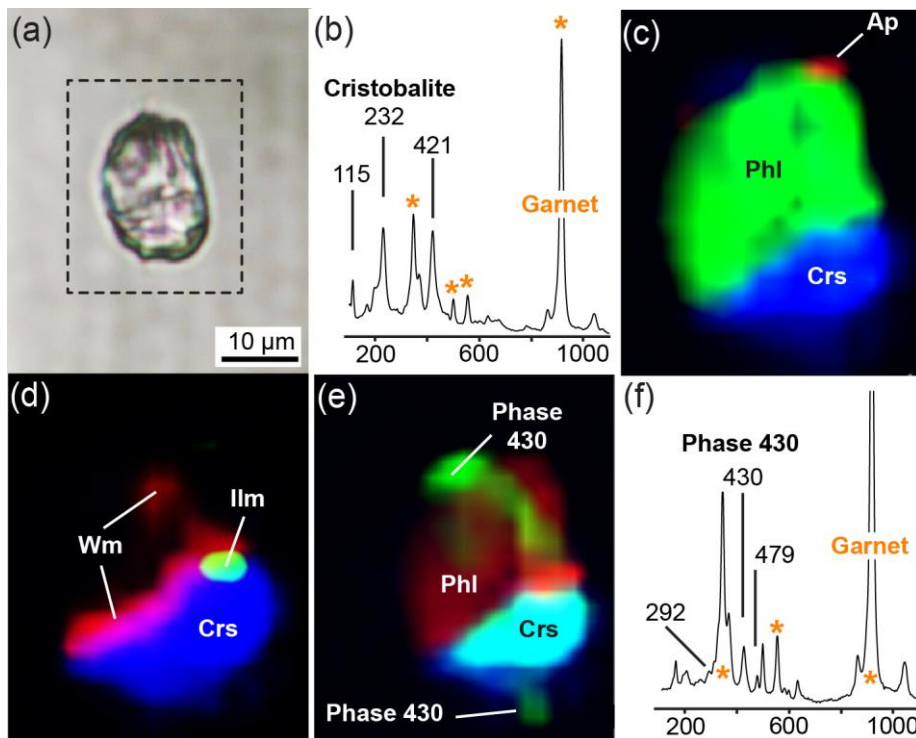


606

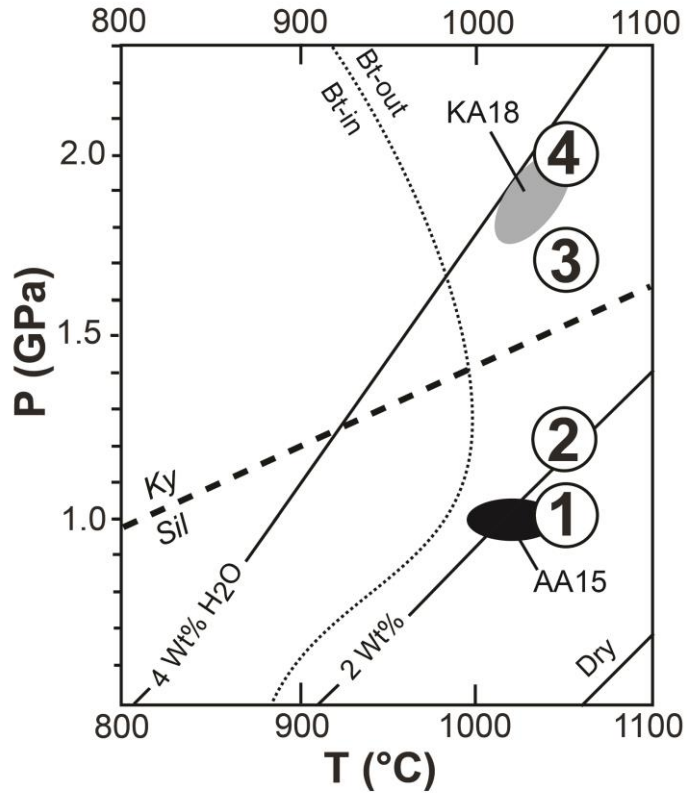
607 FIGURE 1. A) Microstructural features of inclusions and host rocks. (a) Scan of a
 608 representative thin section with garnets in a more felsic matrix; the garnet in the upper left corner
 609 has a circle made with a black marker. *White arrows*: MI-bearing garnets. (b) Cluster of
 610 polycrystalline inclusions occurring in the center of the garnet, mineral abbreviations from
 611 Whitney and Evans (2010). *White arrows*: needle shaped nanogranitoids. *Gray arrows*: isometric
 612 nanogranitoids, generally smaller than the first inclusion type. *Red arrows*: thin rutile needles. (c)

613 Close up of isometric nanogranitoids (**left**) with multiple birefringent phases visible under
 614 crossed polars (**right**). (**d**) Close up of a needle shaped nanogranitoid (**left**), occasionally with the
 615 rough outline already described by Axler and Ague (2015), and showing once again several
 616 birefringent phases under crossed polars (**right**).

617
 618
 619



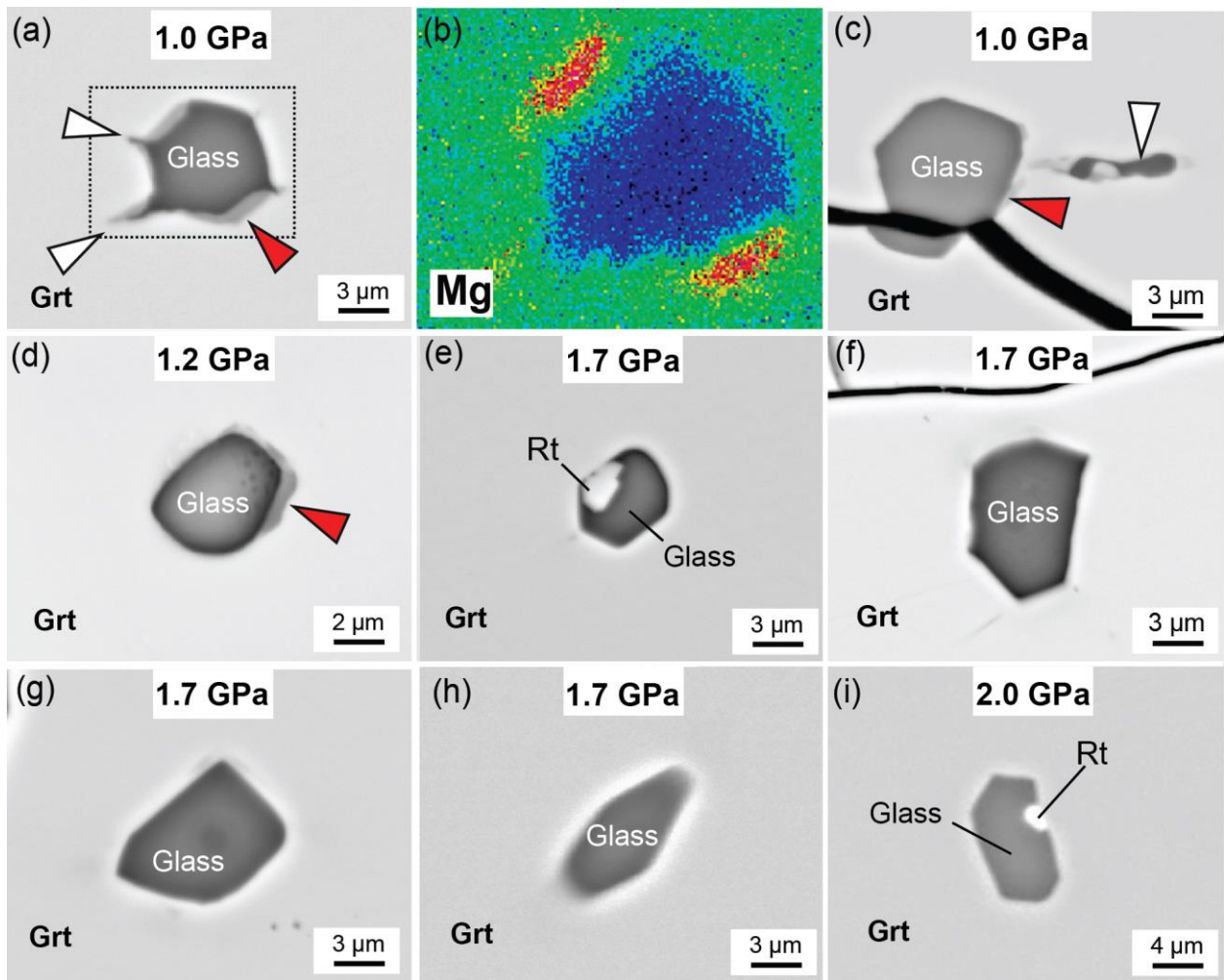
620
 621 **FIGURE 2.** Results of MicroRaman investigation of a representative inclusion below the
 622 surface (**a**). (**b**) Raman spectrum of cristobalite from the CMT nanogranitoids. (**c**) The map
 623 shows the distribution of Raman peak 415 cm^{-1} of cristobalite (blue), 196 cm^{-1} of phlogopite
 624 (963 cm^{-1} of apatite (red). In (**d**) also the distribution of peak 707 of white mica (red)
 625 and the 675 cm^{-1} peak of ilmenite (green) are visible. In (**e**) the distribution of peak 430 cm^{-1} is
 626 visible in green, whereas in (**f**) a representative spectrum of phase 430 is reported.



627
 628 FIGURE 3: Experimental conditions (numbers in circles) versus previous estimates of
 629 metamorphic peak equilibration for the host gneisses of the investigated nanogranitoids. Solid
 630 lines: liquidus curves for different amount of H₂O according to Johannes and Holtz (1996).
 631 AA15: Temperature and minimum P conditions proposed by Axler and Ague (2015) for the felsic
 632 granulites investigated in the present study. KA18: HP conditions estimated on garnet-spinel-
 633 corundum gneisses of the Central Maine Terrane by Keller and Ague (2018).

634

635

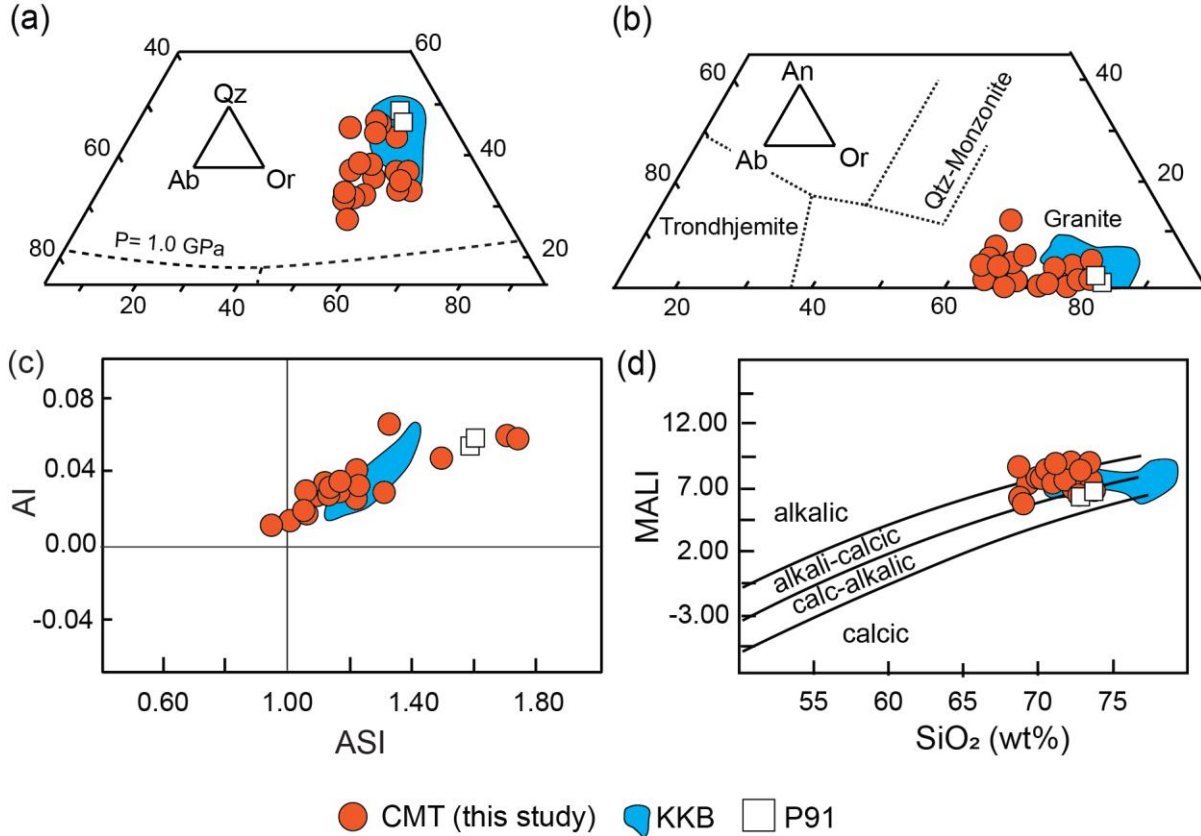


636

637 FIGURE 4. BSE images of CMT nanogranitoids after piston cylinder experiments under
 638 different confining P . *White arrows*: decrepitation cracks. *Red arrows*: new Mg-rich garnet.

639 See text for details on the single images.

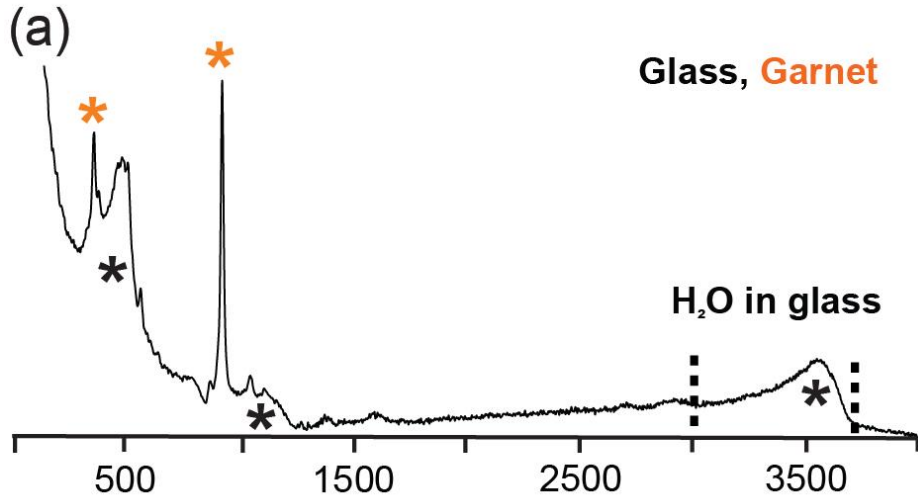
640



642

643

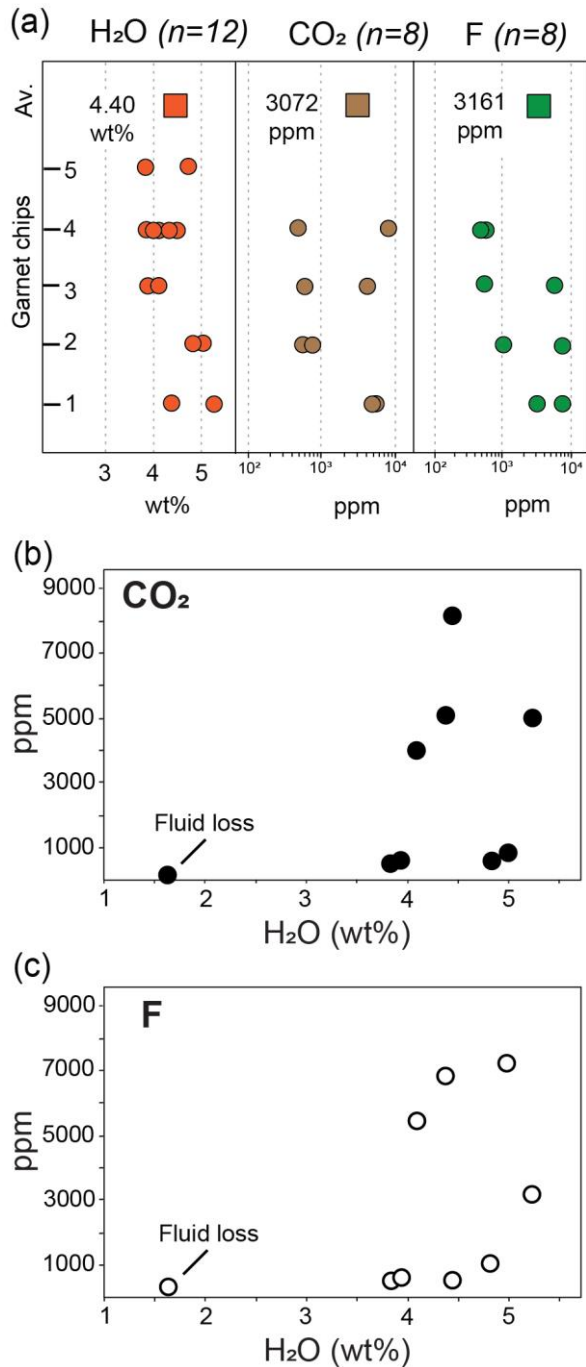
644 FIGURE 5: composition of re-homogenized nanogranitoids. **(a)** Ab-Or-Qz and **(b)** Ab-Or-An
 645 normative diagrams. **(c)** Alumina Saturation Index (ASI)= molar Al/(Ca+Na+K)) versus
 646 Alkalinity Index (AI)= molar Al-(Na+K). **(d)** Silica content versus Modified Alkali-Lime Index
 647 (MALI)= $\text{Na}_2\text{O} + \text{K}_2\text{O} - \text{CaO}$. CMT= central Maine Terrane; KKB= UHT nanogranites of the
 648 Kerala Khondalite Belt (Ferrero et al., 2012). P91= experimental melts from Patiño-Douce and
 649 Johnston (1991). For EMP compositions and P - T conditions of formation of the KKB and P91
 650 melts see Table 2.



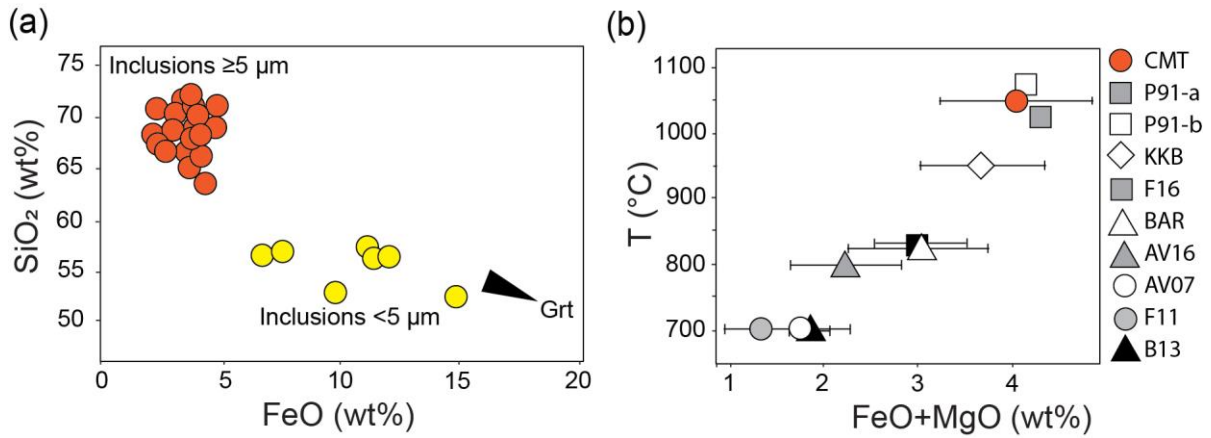
651

652 FIGURE 6: Raman spectrum of nanogranitoid re-homogenized to glass.

653



654
 655 FIGURE 7: NanoSIMS measurements on re-homogenized nanogranitoids. (a) Measurements of
 656 H₂O, CO₂ and F presented according to the garnet chip in which they were measured. Variation
 657 diagrams of (b) CO₂ and (c) F with respect to H₂O for each single NanoSIMS analysis, including
 658 one inclusion with clear fluid loss (indicated in figure).



659
 660 FIGURE 8. High FeO+MgO content in re-homogenized CMT nanogranitoids. (a) Comparison
 661 between inclusion with diameter $\geq 5 \mu\text{m}$ (orange circles) and $< 5 \mu\text{m}$ (yellow circles). (b)
 662 FeO+MgO versus T diagram, comparing nanogranitoids compositions from this study with
 663 previous case studies of inclusions in partially melted rocks with metasedimentary protolith
 664 (including standard deviations; data from Table 2). For abbreviations see caption Table 2.
 665

| Experiment | Figures | T(°C) | P (GPa) | t (h) | Melting | Decrepitation | Melt-host interaction | Full Re-homogenization |
|------------|---------------|-------|---------|-------|---------|---------------|-----------------------|------------------------|
| 1 | Fig. 4a,b,c | 1050 | 1.0 | ≈15 | X | X (extensive) | X (new Grt+New Opx) | - |
| 2 | Fig. 4d | 1050 | 1.2 | 24 | X | - | X (new Grt) | - |
| 3 | Fig. 4e,f,g,h | 1050 | 1.7 | 24 | X | - | - | X |
| 4 | Fig. 4i | 1050 | 2.0 | 24 | X | - | - | X |

666

667

Table 1: Conditions, relevant info and results of piston cylinder experiments.

| Central Maine Terrane | | | | | | | | | | | | | | | | | | | Experiments | | | | | | Other Nanogranitoids | | | | | | | | | | | | |
|------------------------------------|-------|-------|---------|-------|-------|-------|-------|-------|-------|-------|-------|-------|-------|-------|-------|-------|-------|-------|-------------|--------------|--------|-------------|-------------|--------------|----------------------|--------------|--------------|--------------|--------------|--------------|------|------|-----|------|-----|------|--|
| n=19 | 21 | 43 | av.44-4 | 18 | 20 | 21 | 22 | 23 | 24 | 7 | 8 | 32 | 35 | 34 | 3 | 6 | 36 | 39 | 21/22 | Aver. | Stdv | P91 | P91 | KKB | BAR | Stdv | F16 | Stdv | AV16 | Stdv | AV07 | Stdv | F11 | Stdv | B13 | Stdv | |
| Duration | 24h | 24h | 24h | 24h | 24h | 24h | 24h | 24h | 24h | 24h | 24h | 24h | 24h | 24h | 24h | 24h | 24h | 24h | 24h | 4h | | | | | | | | | | | | | | | | | |
| T (°C) | 1050 | 1050 | 1050 | 1050 | 1050 | 1050 | 1050 | 1050 | 1050 | 1050 | 1050 | 1050 | 1050 | 1050 | 1050 | 1050 | 1050 | 1050 | 1050 | 1050 | | | 1025 | 1075 | 950 | 830 | 1050 | 825 | 800 | 700 | 700 | 700 | 700 | 700 | 700 | | |
| P (Gpa) | 1.7 | 1.7 | 1.7 | 1.7 | 1.7 | 1.7 | 1.7 | 1.7 | 1.7 | 1.7 | 1.7 | 1.7 | 1.7 | 2.0 | 2.0 | 2.0 | 2.0 | 2.0 | 2.0 | | | 1.0 | 1.0 | 0.5 | 0.8 | 0.5 | 0.5 | 1.2/1.4 | 0.5 | 0.5 | 0.5 | 0.5 | 0.5 | | | | |
| Wt% | | | | | | | | | | | | | | | | | | | | | Stdv | | | | | | | | | | | | | | | | |
| SiO ₂ | 64.96 | 68.89 | 63.61 | 67.10 | 69.15 | 68.22 | 67.64 | 66.00 | 68.32 | 66.80 | 67.30 | 70.97 | 70.92 | 68.83 | 71.07 | 68.24 | 71.97 | 71.91 | 66.36 | 68.33 | (2.34) | 70.62 | 69.44 | 73.96 (2.63) | 73.77 (2.34) | 70.78 (3.44) | 70.16 (1.29) | 71.23 (1.43) | 68.95 (1.65) | 70.03 (2.28) | | | | | | | |
| TiO ₂ | 0.64 | 0.36 | 0.03 | 0.05 | 0.91 | 0.24 | 0.14 | 0.14 | 0.10 | 0.05 | 0.16 | 0.22 | 0.15 | 0.13 | 0.10 | 0.00 | 0.33 | 0.66 | 0.07 | 0.23 | (0.25) | 0.65 | 0.73 | 0.11 (0.09) | 0.09 (0.08) | 0.06 (0.05) | 0.07 (0.06) | 0.10 (0.03) | 0.10 (0.12) | 0.04 (0.07) | | | | | | | |
| Al ₂ O ₃ | 12.61 | 12.50 | 14.74 | 12.39 | 12.96 | 12.89 | 13.80 | 12.42 | 13.71 | 12.84 | 14.03 | 13.18 | 14.00 | 12.06 | 11.83 | 13.46 | 13.23 | 11.93 | 13.14 | 13.04 | (0.81) | 13.4 | 13.64 | 12.95 (1.31) | 12.90 (1.46) | 11.91 (0.68) | 14.89 (0.98) | 14.44 (0.33) | 12.82 (1.14) | 11.71 (0.86) | | | | | | | |
| FeO | 3.71 | 4.76 | 4.43 | 3.27 | 3.22 | 3.53 | 3.25 | 4.10 | 3.08 | 2.89 | 2.38 | 3.53 | 2.41 | 3.97 | 4.75 | 2.22 | 3.49 | 3.47 | 3.54 | 3.47 | (0.74) | 3.26 | 3.04 | 3.03 (0.69) | 2.51 (0.37) | 2.39 (0.76) | 2.14 (0.59) | 1.71 (0.52) | 1.32 (0.40) | 1.71 (0.21) | | | | | | | |
| MnO | 0.11 | 0.11 | 0.04 | 0.02 | 0.09 | 0.14 | 0.02 | 0.08 | 0.01 | 0.00 | 0.00 | 0.06 | 0.09 | 0.01 | 0.01 | 0.00 | 0.03 | 0.08 | 0.07 | 0.05 | (0.05) | 0.11 | 0.08 | 0.04 (0.03) | 0.25 (0.17) | 0.10 (0.10) | 0.46 (0.07) | 0.08 (0.05) | 0.16 (0.17) | 0.17 (0.10) | | | | | | | |
| MgO | 0.61 | 0.58 | 0.63 | 1.11 | 0.38 | 0.41 | 0.70 | 1.01 | 0.63 | 0.57 | 0.30 | 0.62 | 0.45 | 0.56 | 0.61 | 0.34 | 0.52 | 0.54 | 1.18 | 0.62 | (0.20) | 1.04 | 1.09 | 0.65 (0.21) | 0.53 (0.13) | 0.61 (0.07) | 0.09 (0.02) | 0.05 (0.04) | 0.02 (0.03) | 0.12 (0.07) | | | | | | | |
| CaO | 1.17 | 0.98 | 1.68 | 0.01 | 0.36 | 0.14 | 0.12 | 0.36 | 0.03 | 0.94 | 0.55 | 1.09 | 0.58 | 0.54 | 0.60 | 0.98 | 0.56 | 0.84 | 0.88 | 0.65 | (0.45) | 0.26 | 0.28 | 0.53 (0.20) | 0.85 (0.48) | 1.04 (0.56) | 0.48 (0.13) | 0.60 (0.09) | 0.68 (0.16) | 0.45 (0.13) | | | | | | | |
| Na ₂ O | 1.32 | 1.28 | 1.58 | 1.71 | 1.28 | 1.50 | 1.66 | 1.17 | 1.14 | 1.89 | 1.68 | 2.11 | 2.17 | 2.29 | 2.45 | 3.03 | 2.68 | 0.96 | 1.52 | 1.76 | (0.58) | 0.79 | 0.84 | 1.10 (0.32) | 1.94 (0.13) | 0.57 (0.45) | 2.88 (1.24) | 3.63 (0.39) | 2.25 (0.35) | 2.79 (0.35) | | | | | | | |
| K ₂ O | 6.93 | 7.00 | 5.11 | 6.10 | 7.23 | 7.17 | 4.71 | 5.23 | 5.51 | 6.01 | 7.41 | 5.81 | 6.68 | 6.18 | 6.07 | 6.69 | 6.51 | 6.45 | 6.13 | 6.26 | (0.78) | 5.98 | 6.05 | 6.72 (0.70) | 4.86 (0.79) | 6.24 (1.10) | 3.97 (1.00) | 4.97 (0.31) | 4.56 (0.83) | 4.05 (0.39) | | | | | | | |
| P ₂ O ₅ | 0.59 | 0.75 | 0.28 | 0.05 | 0.18 | 0.15 | 0.16 | 0.12 | 0.07 | 0.23 | 0.19 | 0.17 | 0.07 | 0.07 | 0.00 | 0.12 | 0.25 | 0.20 | 0.38 | 0.21 | (0.19) | 0.11 | 0.06 | 0.03 (0.05) | 0.02 (0.02) | 0.28 (0.09) | 0.01 (0.01) | 0.37 (0.09) | 0.16 (0.07) | 0.26 (0.23) | | | | | | | |
| Cl | 0.07 | 0.21 | 0.08 | 0.86 | 0.82 | 0.68 | 0.95 | 0.93 | 0.97 | 0.01 | 0.04 | 0.00 | 0.01 | 0.09 | 0.10 | 0.10 | 0.10 | 0.00 | 0.01 | 0.32 | (0.39) | - | - | - | - | - | - | - | - | - | - | - | - | - | - | - | |
| Total | 92.64 | 97.21 | 92.12 | 91.79 | 95.76 | 94.38 | 92.20 | 90.62 | 92.59 | 96.17 | 98.00 | 97.76 | 97.53 | 94.64 | 97.49 | 99.07 | 99.57 | 97.05 | 93.29 | 95.37 | | 96.22 | 95.25 | 99.12 | 97.73 | 93.97 | 95.15 | 97.16 | 91.02 | 91.33 | | | | | | | |
| Q | 26 | 30 | 27 | 29 | 31 | 29 | 36 | 34 | 37 | 32 | 30 | 31 | 29 | 27 | 27 | 25 | 27 | 37 | 29 | 30 | | 39 | 37 | 37 | 39 | 39 | 35 | 29 | 36 | 36 | | | | | | | |
| C | 2 | 3 | 4 | 3 | 3 | 3 | 6 | 4 | 6 | 2 | 2 | 2 | 2 | 1 | 0 | 0 | 1 | 2 | 3 | 3 | | 5 | 5 | 3 | 3 | 3 | 5 | 3 | 3 | 3 | | | | | | | |
| Or | 41 | 41 | 30 | 36 | 43 | 42 | 28 | 31 | 33 | 37 | 45 | 34 | 39 | 37 | 36 | 41 | 38 | 38 | 36 | 37 | | 35 | 36 | 40 | 29 | 37 | 23 | 29 | 27 | 24 | | | | | | | |
| Ab | 11 | 11 | 13 | 14 | 11 | 13 | 14 | 10 | 10 | 15 | 14 | 18 | 18 | 19 | 21 | 25 | 23 | 8 | 13 | 15 | | 7 | 7 | 9 | 16 | 5 | 24 | 31 | 19 | 24 | | | | | | | |
| An | 2 | 0 | 7 | 0 | 1 | 0 | 0 | 1 | 0 | 3 | 1 | 4 | 2 | 2 | 3 | 3 | 1 | 3 | 2 | 2 | | 1 | 1 | 2 | 4 | 3 | 2 | 1 | 2 | 1 | | | | | | | |
| Hy | 7 | 10 | 10 | 9 | 6 | 7 | 8 | 10 | 7 | 7 | 5 | 8 | 5 | 8 | 10 | 4 | 7 | 7 | 9 | 7 | | 8 | 7 | 7 | 6 | 6 | 5 | 3 | 3 | 4 | | | | | | | |
| ASI | 1.07 | 1.09 | 1.32 | 1.31 | 1.22 | 1.23 | 1.71 | 1.51 | 1.74 | 1.11 | 1.16 | 1.12 | 1.18 | 1.05 | 1.01 | 0.95 | 1.06 | 1.18 | 1.22 | 1.22 | | 1.63 | 1.62 | 1.29 | 1.29 | 1.24 | 1.50 | 1.16 | 1.30 | 1.19 | | | | | | | |
| H ₂ O by diff | 7.36 | 2.79 | 7.88 | 8.21 | 4.24 | 5.62 | 7.80 | 9.38 | 7.41 | 3.83 | 2.00 | 2.24 | 2.47 | 5.36 | 2.51 | 0.93 | 0.43 | 2.95 | 6.72 | 4.63 | | 3.78 | 4.75 | 0.88 | 2.27 | 6.03 | 4.85 | 2.84 | 8.98 | 8.67 | | | | | | | |
| Mg# | 0.22 | 0.18 | 0.20 | 0.38 | 0.17 | 0.16 | 0.27 | 0.30 | 0.27 | 0.26 | 0.18 | 0.24 | 0.24 | 0.20 | 0.19 | 0.21 | 0.21 | 0.37 | 0.23 | | 0.35 | 0.38 | 0.27 | 0.26 | 0.30 | 0.06 | 0.04 | 0.03 | 0.10 | | | | | | | | |
| FeO+MgO+TiO ₂ | 4.95 | 5.69 | 5.08 | 4.42 | 4.51 | 4.17 | 4.09 | 5.24 | 3.80 | 3.51 | 2.84 | 4.36 | 3.02 | 4.66 | 5.46 | 2.56 | 4.34 | 4.67 | 4.79 | 4.30 | | 4.95 | 4.86 | 3.79 | 3.13 | 3.05 | 2.30 | 1.86 | 1.44 | 1.87 | | | | | | | |
| FeO+MgO | 4.31 | 5.34 | 5.05 | 4.37 | 3.60 | 3.94 | 3.95 | 5.11 | 3.70 | 3.47 | 2.67 | 4.15 | 2.86 | 4.53 | 5.36 | 2.56 | 4.01 | 4.01 | 4.72 | 4.05 | | 3.94 | 3.92 | 3.68 | 3.04 | 2.99 | 2.23 | 1.76 | 1.34 | 1.83 | | | | | | | |
| K ₂ O/Na ₂ O | 5.24 | 5.48 | 3.24 | 3.57 | 5.64 | 4.79 | 2.84 | 4.48 | 4.82 | 3.18 | 4.41 | 2.76 | 3.07 | 2.69 | 2.48 | 2.21 | 2.43 | 6.71 | 4.04 | 3.89 | | 7.57 | 7.20 | 6.09 | 2.51 | 11.01 | 1.38 | 1.37 | 2.02 | 1.45 | | | | | | | |

668

669 Table 2: Geochemistry and PT conditions of formation of re-homogenized melt inclusions from the Central Maine Terrane, high
670 temperature experimental melts from metasediments (P91= Patiño-Douce and Johnston, 1991) and averages of melt inclusion analyses
671 from different case studies of metasediments melted under different conditions. KKB (Kerala Khondalite Belt, Southern India) and BAR
672 (Barun gneiss, Himalaya) are from Ferrero et al., (2012). F16 = Oberpfalz migmatites from Ferrero et al. (2016). AAV16= Jubrique
673 migmatites, Betic Cordillera (S Spain) from Acosta-Vigil et al., (2016). AAV07= Grt+Bt granulitic enclaves of El Hoyazo, Neogene
674 Volcanic Province (S Spain) from Acosta-Vigil et al., (2007). F11= Spl-Crd granulitic enclaves of El Hoyazo from Ferrero et al. (2011).
675 B13= Sierra Alpujata metatexites, Betic Cordillera (S Spain) from Bartoli et al., (2013).

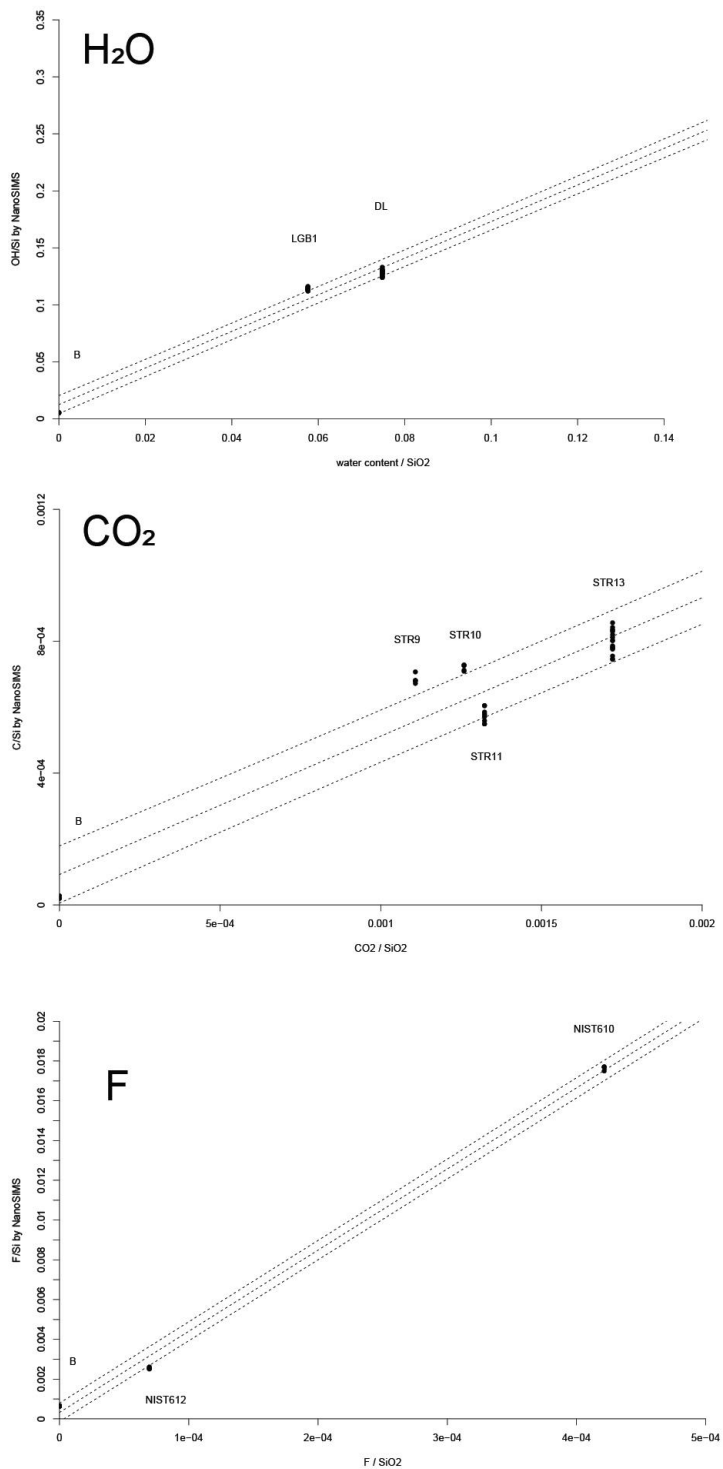
676

677

| Garnet | Analysis | H ₂ O (wt.%) | 1 σ error | CO ₂ (ppm) | 1 σ error | F (ppm) | 1 σ error |
|--------|------------|----------------------------|---------------------|--------------------------|---------------------|------------|---------------------|
| 1 | Exp4_M1_1 | 4.38 | 0.05 | 5073 | 204 | 6820 | 106 |
| | Exp4_M4_1 | 5.24 | 0.06 | 4979 | 201 | 3198 | 49 |
| 2 | Exp4_M2_1 | 4.83 | 0.05 | 538 | 32 | 1033 | 15 |
| | Exp4_M3_1 | 5.00 | 0.05 | 790 | 34 | 7223 | 112 |
| 3 | Exp3_MI_2 | 3.93 | 0.05 | 603 | 34 | 541 | 8 |
| | Exp3_MI_6 | 4.09 | 0.05 | 3983 | 164 | 5462 | 85 |
| 4 | Exp3_MI_3 | 4.46 | 0.05 | 8109 | 339 | 535 | 8 |
| | Exp3_MI_1 | 1.64 | 0.07 | 113 | 38 | 79 | 2 |
| | Exp3_tub_1 | 3.85 | 0.05 | 504 | 32 | 479 | 7 |
| | Exp3_1 | 4.18 | 0.17 | | | | |
| | Exp3_2 | 4.29 | 0.17 | | | | |
| 5 | Exp3_3 | 3.84 | 0.17 | | | | |
| | Exp3_4 | 4.69 | 0.17 | | | | |

678

679 Table 3. H₂O, CO₂ and F contents in re-homogenized inclusions measured by NanoSIMS.



681

682 Figure S1. Calibration curves for NanoSIMS measurements.

| Analyses | 24 | 36 | 59 | 60 | 61 | 62 | 64 |
|--------------------------------|-----------|-----------|-----------|-----------|-----------|-----------|-----------|
| Duration | 24h |
| T (°C) | 1050 | 1050 | 1050 | 1050 | 1050 | 1050 | 1050 |
| P (GPa) | 1.0 | 1.0 | 1.2 | 1.2 | 1.2 | 1.2 | 1.2 |
| Wt% | | | | | | | |
| SiO ₂ | 56.42 | 57.42 | 56.95 | 56.52 | 52.89 | 56.33 | 52.55 |
| TiO ₂ | 0.78 | 0.00 | 0.01 | 0.13 | 0.00 | 0.39 | 0.05 |
| Al ₂ O ₃ | 14.75 | 18.67 | 13.87 | 16.58 | 13.89 | 14.77 | 15.49 |
| FeO | 12.01 | 11.13 | 7.45 | 6.71 | 9.86 | 11.41 | 14.91 |
| MnO | 0.11 | 0.11 | 0.04 | 0.02 | 0.09 | 0.14 | 0.08 |
| MgO | 1.24 | 4.67 | 2.78 | 3.17 | 2.94 | 3.28 | 4.36 |
| CaO | 2.66 | 0.99 | 0.86 | 1.55 | 1.05 | 1.34 | 1.26 |
| Na ₂ O | 3.43 | 1.08 | 1.08 | 1.33 | 0.89 | 1.23 | 0.88 |
| K ₂ O | 3.48 | 4.20 | 4.98 | 5.75 | 5.03 | 3.10 | 3.47 |
| P ₂ O ₅ | 1.72 | 0.12 | 1.78 | 0.04 | 0.12 | 0.16 | 0.16 |
| Cl | 0.07 | 0.21 | 0.08 | 0.86 | 0.82 | 0.68 | 0.93 |
| Total | 96.49 | 98.65 | 89.74 | 91.78 | 86.67 | 92.00 | 93.13 |

684

685 Table S1. EMP analyses of inclusions <5 μm in diameter.

686

687